

Article

Effects of Bi Substitution on the Cobalt-Free 60wt.%Ce_{0.9}Pr_{0.1}O_{2-δ}-40wt.%Pr_{0.6}Sr_{0.4}Fe_{1-x}Bi_xO_{3-δ} Oxygen Transport Membranes

Chao Zhang ¹, Yanhao Huang ¹, Lingyong Zeng ¹, Yiyi He ¹, Peifeng Yu ¹ and Huixia Luo ^{1,2,3,4,*}

- ¹ School of Materials Science and Engineering, Sun Yat-Sen University, No. 135, Xingang Xi Road, Guangzhou 510275, China; zhangch259@mail2.sysu.edu.cn (C.Z.); huangyh296@mail2.sysu.edu.cn (Y.H.); zengly25@mail2.sysu.edu.cn (L.Z.); heyy39@mail2.sysu.edu.cn (Y.H.); yupf3@mail2.sysu.edu.cn (P.Y.)
- ² State Key Laboratory of Optoelectronic Materials and Technologies, No. 135, Xingang Xi Road, Guangzhou 510275, China
- ³ Key Lab of Polymer Composite & Functional Materials, Sun Yat-Sen University, No. 135, Xingang Xi Road, Guangzhou 510275, China
- ⁴ Guangzhou Key Laboratory of Flexible Electronic Materials and Wearable Devices, Sun Yat-Sen University, No. 135, Xingang Xi Road, Guangzhou 510275, China
- * Correspondence: luohx7@mail.sysu.edu.cn; Tel.: +86-020-3938-6124

Abstract: The mixed ionic-electronic conducting (MIEC) oxygen transport membrane (OTM) can completely selectively penetrate oxygen theoretically and can be widely used in gas separation and oxygen-enriched combustion industries. In this paper, dual-phase MIEC OTMs doped with Bi are successfully prepared by a sol-gel method with high-temperature sintering, whose chemical formulas are 60wt.%Ce_{0.9}Pr_{0.1}O_{2-δ}-40wt.%Pr_{0.6}Sr_{0.4}Fe_{1-x}Bi_xO_{3-δ} (60CPO-40PSF_{1-x}B_xO, $x = 0.01, 0.025, 0.05, 0.10, 0.15, 0.20$). The dual-phase structure, element content, surface morphology, oxygen permeability, and stability are studied by XRD, EDXS, SEM, and self-built devices, respectively. The optimal Bi-doped component is 60wt.%Ce_{0.9}Pr_{0.1}O_{2-δ}-40wt.%Pr_{0.6}Sr_{0.4}Fe_{0.99}Bi_{0.01}O_{3-δ}, which can maintain 0.71 and 0.62 mL·min⁻¹·cm⁻² over 50 h under He and CO₂ atmospheres, respectively. The oxygen permeation flux through these Bi-doped OTMs under air/CO₂ gradient is 12.7% less than that under air/He gradient, which indicates that the Bi-doped OTMs have comparable oxygen permeability and excellent CO₂ tolerance.

Keywords: oxygen transport membrane; dual-phase membrane; mixed conducting; Bi substitution; CO₂ tolerance



Citation: Zhang, C.; Huang, Y.; Zeng, L.; He, Y.; Yu, P.; Luo, H. Effects of Bi Substitution on the Cobalt-Free 60wt.%Ce_{0.9}Pr_{0.1}O_{2-δ}-40wt.%Pr_{0.6}Sr_{0.4}Fe_{1-x}Bi_xO_{3-δ} Oxygen Transport Membranes. *Processes* **2021**, *9*, 1767. <https://doi.org/10.3390/pr9101767>

Academic Editor: Federica Raganati

Received: 26 August 2021

Accepted: 28 September 2021

Published: 1 October 2021

Publisher's Note: MDPI stays neutral with regard to jurisdictional claims in published maps and institutional affiliations.



Copyright: © 2021 by the authors. Licensee MDPI, Basel, Switzerland. This article is an open access article distributed under the terms and conditions of the Creative Commons Attribution (CC BY) license (<https://creativecommons.org/licenses/by/4.0/>).

1. Introduction

Atmospheric management is gaining importance in the era of climate warming. The mixed ionic-electronic conducting (MIEC) oxygen transport membrane (OTM) is an environmentally friendly and efficient air separation membrane, which can effectively separate O₂ and capture CO₂ based on the oxy-fuel concept [1–3], as well as employing membrane reactors for catalytic reactions such as partial oxidation of methane, methane aromatization, water splitting, and so on [4–7].

Over the past decades, researchers have been engaged in the development of single-type perovskite-related structure oxide OTMs. In fact, these single-type perovskite materials (e.g., Ba_{0.5}Sr_{0.5}Fe_{0.8}Co_{0.2}O_{3-δ}) possess high ambipolar conductivities accompanying high oxygen permeabilities at high temperatures [8–10]. However, most of the single-type perovskite OTMs containing alkali earth metal elements in the A-site, such as Ba, are easy to form a carbonate impurity phase at high temperature under CO₂ atmosphere, which reduces the stability and oxygen permeability of the membranes [10]. On the other hand, single-type perovskite OTMs containing Co in the B-site have a large expansion coefficient at high temperatures, which reduces the structural stability of the OTMs [8,11,12].

Therefore, these oxygen-permeable membranes containing Ba or Co usually have superior oxygen permeability, and yet they are limited to widespread practical applications due to their poor chemical/mechanical stabilities [13–15].

In order to maintain high oxygen permeability, as far as possible, to improve the stability of OTMs, many studies have been performed. For example, rare earth metal cations such as La and Pr were used to partially doped alkali earth metal elements in the *A*-site, and the content of Co in the *B*-site was reduced [16]. On the other hand, dual-phase OTMs, which consist of both the oxygen ion conductor (fluorite phase) and the electron conductor (perovskite phase), were considered to be an alternative for the single-type OTMs. However, although the dual-phase OTMs exhibit enhanced stability, they usually have insufficient oxygen permeability [17]. Recently, our group has employed the stronger acidity (or weaker alkalinity, according to Lewis acid-base theory) or more stable transition metal elements to partially replace the original transition metal elements in *B*-site, and successfully developed a series of Fe-based cobalt-free dual-phase OTMs (e.g., $\text{Ce}_{0.85}\text{Pr}_{0.1}\text{Cu}_{0.05}\text{O}_{2-\delta}$ - $\text{Pr}_{0.6}\text{Sr}_{0.4}\text{Fe}_{1-x}\text{Cu}_x\text{O}_{3-\delta}$, $\text{Ce}_{0.9}\text{Pr}_{0.1}\text{O}_{2-\delta}$ - $\text{Pr}_{0.6}\text{Sr}_{0.4}\text{Fe}_{1-x}\text{Al}_x\text{O}_{3-\delta}$) [18–20], which show improvement of oxygen permeability and can retain the stability. Table 1 shows the oxygen permeation flux and stability test time of some related OTMs. From Table 1, we can see that our Bi-containing OTMs show comparable oxygen permeation flux and CO_2 stability.

Table 1. The oxygen flux and stability test time of some related OTMs at CO_2 atmosphere.

Materials	Thickness (mm)	$J(\text{O}_2)$ ($\text{mL}\cdot\text{min}^{-1}\cdot\text{cm}^{-2}$)	Test Time	T ($^\circ\text{C}$)	Refs.
60wt.% $\text{Ce}_{0.9}\text{Pr}_{0.1}\text{O}_{2-\delta}$ -40wt.% $\text{Pr}_{0.6}\text{Sr}_{0.4}\text{Fe}_{0.99}\text{Bi}_{0.01}\text{O}_{3-\delta}$	0.6	0.62	50 h	1000	This work
60wt.% $\text{Ce}_{0.9}\text{Pr}_{0.1}\text{O}_{2-\delta}$ -40wt.% $\text{Pr}_{0.6}\text{Sr}_{0.4}\text{FeO}_{3-\delta}$	0.6	0.22	100 h	950	[17]
60wt.% $\text{Ce}_{0.9}\text{Pr}_{0.1}\text{O}_{2-\delta}$ -40wt.% $\text{Pr}_{0.6}\text{Sr}_{0.4}\text{Fe}_{0.5}\text{Co}_{0.5}\text{O}_{3-\delta}$	0.6	0.7	400 h	950	[21]
60wt.% $\text{Ce}_{0.9}\text{Pr}_{0.1}\text{O}_{2-\delta}$ -40wt.% $\text{Pr}_{0.6}\text{Sr}_{0.4}\text{Fe}_{0.6}\text{Al}_{0.4}\text{O}_{3-\delta}$	0.4	1.12 (He)	25 h	1000	[18]
60wt.% $\text{Ce}_{0.9}\text{Pr}_{0.1}\text{O}_{2-\delta}$ -40wt.% $\text{Pr}_{0.6}\text{Sr}_{0.4}\text{Fe}_{0.99}\text{In}_{0.01}\text{O}_{3-\delta}$	0.6	0.80	100 h	1000	[22]
60wt.% $\text{Ce}_{0.9}\text{Nd}_{0.1}\text{O}_{2-\delta}$ -40wt.% $\text{Pr}_{0.6}\text{Nd}_{0.4}\text{FeO}_{3-\delta}$	0.6	0.48	120 h	1000	[23]
60wt.% $\text{Ce}_{0.9}\text{Nd}_{0.1}\text{O}_{2-\delta}$ -40wt.% $\text{Pr}_{0.6}\text{Nd}_{0.4}\text{Al}_{0.2}\text{Fe}_{0.8}\text{O}_{3-\delta}$	0.6	0.52	100 h	1000	[24]
$\text{Pr}_{0.6}\text{Sr}_{0.4}\text{Co}_{0.2}\text{Fe}_{0.8}\text{O}_{3-\delta}$	0.6	1.24	200 h	1000	[16]
$\text{BaBi}_{0.05}\text{Co}_{0.8}\text{Nb}_{0.15}\text{O}_{3-\delta}$	1.3	2.92 (He)	-	900	[25]
$\text{BaCo}_{0.85}\text{Bi}_{0.05}\text{Zr}_{0.1}\text{O}_{3-\delta}$	1.51/1.04 (Fiber)	2.05	12 h	900	[26]

Bismuth (Bi), with the electron configuration of $4f^{14}5d^{10}6s^26p^3$, belongs to the group VA of the sixth cycle, in which the two electrons of the 6s orbital are difficult to be lost due to the inert electron effect caused by the strong penetration effect of the 6s orbital. Thus, Bi^{3+} is a stable valence state [27], which is similar to Al^{3+} [28] and can produce oxygen vacancies when doped to the *B*-site. Moreover, at high temperatures, $\delta\text{-Bi}_2\text{O}_3$ contains a large number of oxygen vacancies, which is an excellent oxygen ion conductor and is conducive to the diffusion and transmission of oxygen in the OTMs [29–31]. In addition, Bi_2O_3 is often used as a catalyst [9,32,33]. For example, Liu et al. reported that the nano Bi_2O_3 was a high-effective catalyst for electroreduction of CO_2 to HCOOH [9]. Based on these previous studies, it is a natural question to ask whether the Bi substitution for Fe-site in $60\text{wt.}\%\text{Ce}_{0.9}\text{Pr}_{0.1}\text{O}_{2-\delta}$ - $40\text{wt.}\%\text{Pr}_{0.6}\text{Sr}_{0.4}\text{FeO}_{3-\delta}$ could bring in improved oxygen permeation performance.

In this paper, we design a group of bismuth-doping cobalt-free dual-phase OTMs with compositions of $60\text{wt.}\%\text{Ce}_{0.9}\text{Pr}_{0.1}\text{O}_{2-\delta}$ - $40\text{wt.}\%\text{Pr}_{0.6}\text{Sr}_{0.4}\text{Fe}_{1-x}\text{Bi}_x\text{O}_{3-\delta}$ ($60\text{CPO-}40\text{PSF}_{1-x}\text{B}_x\text{O}$, $x = 0.01, 0.025, 0.05, 0.10, 0.15, 0.20$), which is synthesized via a sol-gel method. Effects of Bi substitution on phase structures and the oxygen permeability as well as stability are explored in detail.

2. Experimental

2.1. Powders and Membranes Preparation

60wt.%Ce_{0.9}Pr_{0.1}O_{2-δ}-40wt.%Pr_{0.6}Sr_{0.4}Fe_{1-x}Bi_xO_{3-δ} (60CPO-40PSF_{1-x}B_xO, $x = 0.01, 0.025, 0.05, 0.10, 0.15, 0.20$) powders were prepared by a sol-gel method. Firstly, the stoichiometric ratios of the nitrates were dissolved into the deionized water. The citric acid monohydrate and ethylene glycol were added as chelating agents and surfactants, respectively. After evaporation, the colloids were dried at 140 °C for 24 h and ground to powders. For removing organic impurities, the powders would be calcined at 600 °C for 8 h. After regrinding, the obtained powders were heated at 950 °C for 5 h to prepare 60CPO-40PSF_{1-x}B_xO ($x = 0.01, 0.025, 0.05, 0.10, 0.15, 0.20$) powders. The powders were pressed in a 15 mm diameter circular mold at about 10 MPa and sintered at the best temperature (1400 °C for $x = 0.01, 0.025, \text{ and } 0.05$, 1350 °C for $x = 0.10 \text{ and } 0.15$, 1300 °C for $x = 0.20$), with 1 °C/min rate to form a dense dual-phase OTMs. Finally, all the OTMs were polished into the thickness of 0.6 mm with different mesh sandpapers.

2.2. Characterization of Membranes

Powder X-ray diffraction (XRD, Rigaku with Cu K α , Japan) was used to characterize the structure of 60CPO-40PSF_{1-x}B_xO dual-phase powders in the 2 θ range of 10–100° with a scanning speed of 0.5°/min and an interval of 0.02°. The XRD data were refined by the FullProf Suite software with Rietveld fitting model, and the crystal structure model was made by Vesta software according to XRD refinement [34]. The surface microstructures and phase distribution of the membranes were characterized by scanning electron microscope (SEM, COXEM EM-30AX, Beijing, China), energy-dispersive X-ray spectroscopy (EDXS), and backscattered scanning electron microscopy (BSEM).

2.3. Oxygen Permeability of Membranes

A high-temperature device made up of a corundum tube and vertical tubular furnace [35,36] was used to measure the oxygen permeability of 60CPO-40PSF_{1-x}B_xO OTMs. The polished OTM was sealed by the high-temperature sealant (Huitian 2767, Hubei, China) at one end of the corundum tube and put into the device. The effective area of OTMs is about 0.7 cm². During the oxygen permeation test, 150 mL·min⁻¹ synthetic air was used to be the feed gas. A total of 49 mL·min⁻¹ He/CO₂ and 1 mL·min⁻¹ Ne were flowed into the sweep side as the sweep gas and calibration gas, respectively. All the fluxes of gases were regulated by the mass flow meters (Sevenstar, Beijing, China). The oxygen permeability was measured by the gas chromatograph (GC, PANNA-A60, Changzhou, China), which could obtain concentrations of various gases in the sweep side. The oxygen permeation flux (J_{O_2}) included the leakage of oxygen and could be calculated with the following Equation (1) [18,37,38]:

$$J_{O_2} = (C_{O_2} - \frac{C_{N_2}}{4.02}) \times \frac{F}{S} \quad (1)$$

where C_{O_2} and C_{N_2} are the concentration of O₂ and N₂, respectively. C_{N_2} divided by 4.02 represents the leakage part in C_{O_2} , F represents the total gas flux, and S is the effective area of the OTM.

3. Results and Discussion

3.1. Phase Structural Characterization

XRD was used to determine the phase structure of 60CPO-40PSF_{1-x}B_xO powders, and the results were fitted by FullProf Suite software. Figure 1 shows the XRD patterns of 60CPO-40PSF_{1-x}B_xO dual-phase powders. All the powders consist of the CPO phase (space group: Fm-3m, fluorite phase) and PSFBO phase (space group: Pnma, perovskite phase) without any impurity phase. Figure 2 shows the structure models of the two phases, drawn by VESTA software [34]. The perovskite phase is not cubic because of the small tolerance factor. Generally, when the tolerance factor is between 0.79 and 0.90,

the phase is orthogonal. As shown in Supplementary Figure S1, as x increases from 0 to 0.20, the tolerance factor decreases from 0.8487 to 0.8122 (calculated with the formula in reference [39]). The tolerance factor far from 1 makes the perovskite phase tend to form an orthogonal structure.

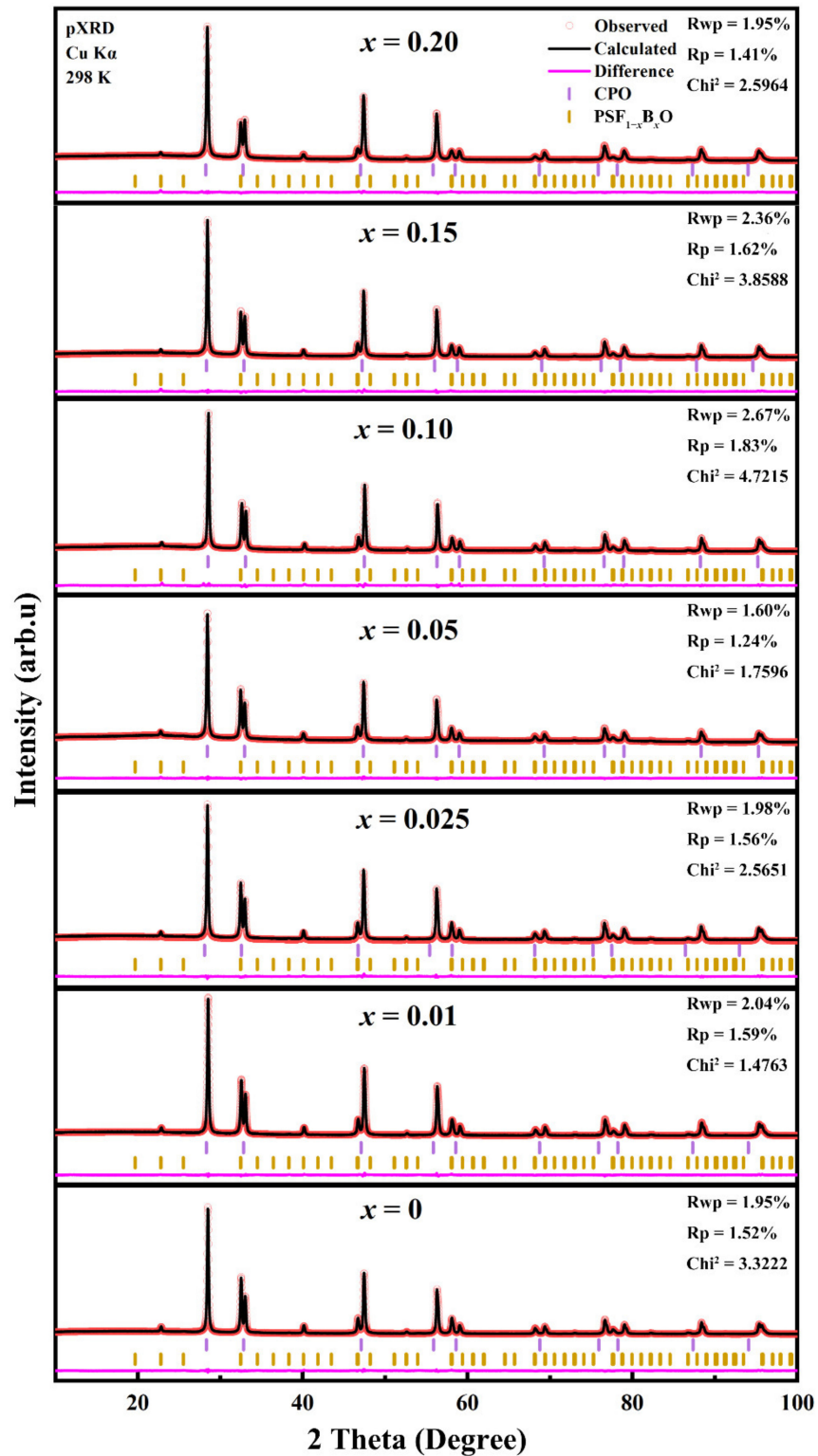


Figure 1. XRD patterns of 60CPO-40PSF_{1-x}B_xO ($x = 0, 0.01, 0.025, 0.05, 0.10, 0.15, 0.20$) powders obtained by calcined at 950 °C for 10 h.

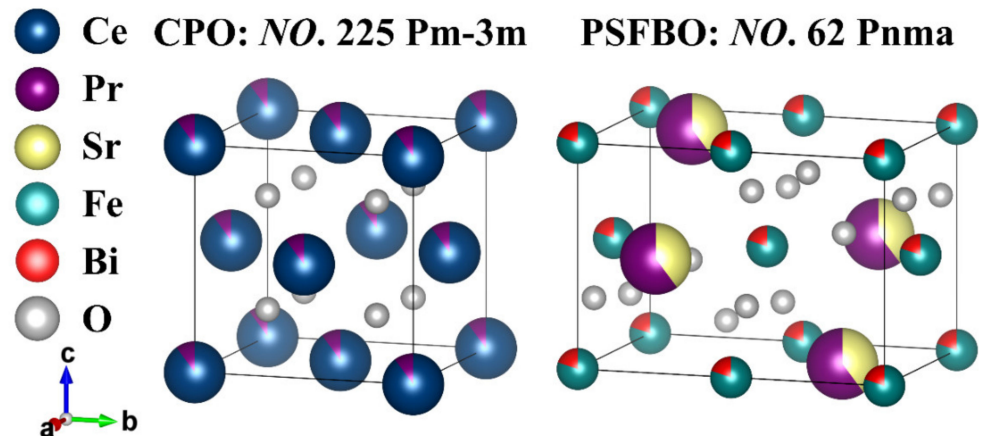


Figure 2. Crystal structure models of 60CPO-40PSF_{1-x}B_xO.

3.2. Surface Morphology Characterization

Maintaining the heating rate (cooling rate) of 1 °C/min and sintering time of 5 h, OTMs with different Bi doping content (x) have different optimal sintering temperatures. As shown in Supplementary Figure S1, the optimal sintering temperature for these 60CPO-40PSF_{1-x}B_xO membranes appears to decline when $x \geq 0.1$ and decreases by up to 100 °C at $x = 0.20$. On the one hand, the reason could be that the melting point of bismuth oxide is lower than the oxide of iron in the parent material, causing a decrease in sintering temperature in molten sintering, and the results are similar to those of Cu doping [19,40]. On the other hand, it can also be explained by the calculation of the reduced average bond energy (ABE) of the system in Section 3.3, which is possibly correlated with the enthalpy of formation.

We tested the volume density of the sintered dual-phase membranes with the Archimedes method, and the results are shown in Table S1. By comparing the theoretical density obtained by fitting the powder XRD results, the relative density of the sintered dual-phase membrane is calculated. Although the sintering temperature of the membranes ($x = 0.10, 0.15,$ and 0.20) is different, the membranes all have a suitable relative density (>90%).

The surface morphological characteristics and elemental distribution characteristics of the sintered 60CPO-40PSF_{1-x}B_xO OTMs are characterized by SEM, BSEM, and EDXS. According to the SEM and BSEM images presented in Figure 3, the surfaces of the sintered OTMs at the optimal temperature are almost free of holes and cracks, which ensures the density of the OTMs. Grains and grain boundaries of the CPO and PSFBO phases can be observed in both SEM and BSEM images. The grain size is uniform, which is about 1 μm and favorable for the transport of electrons and oxygen ions. The bright and dark areas in the BSEM image are fluorite phases (CPO) and perovskite phases (PSFBO), respectively, because the fluorite phase (CPO) has a larger elemental mass and produces more backscattered electrons.

In this case, we chose the OTMs obtained from the optimal sintering temperature for further oxygen permeability study. So far, we have not studied the effect of different temperatures on the oxygen flux. However, based on the previous literature, we propose that the effect of sintering temperature on the oxygen flux mainly comes from its effect on the surface morphology, grain size, relative density, and phase distribution of OTMs [37,41]. For example, in the Fe₂O₃-Ce_{0.9}Gd_{0.1}O_{2- δ} case, the oxygen permeation fluxes decrease with increasing sintering temperature, i.e., increasing grain size [41]. However, in our case, the other sintering temperatures are hard to obtain dense 60CPO-40PSF_{1-x}B_xO OTMs, which leads to hard to seal the OTMs. On the other hand, the membranes with different doping content obtained different optimal sintering temperatures show similar grain sizes around 1 μm . Thus, we only focus on the effect of doping content on the oxygen permeation flux in this case.

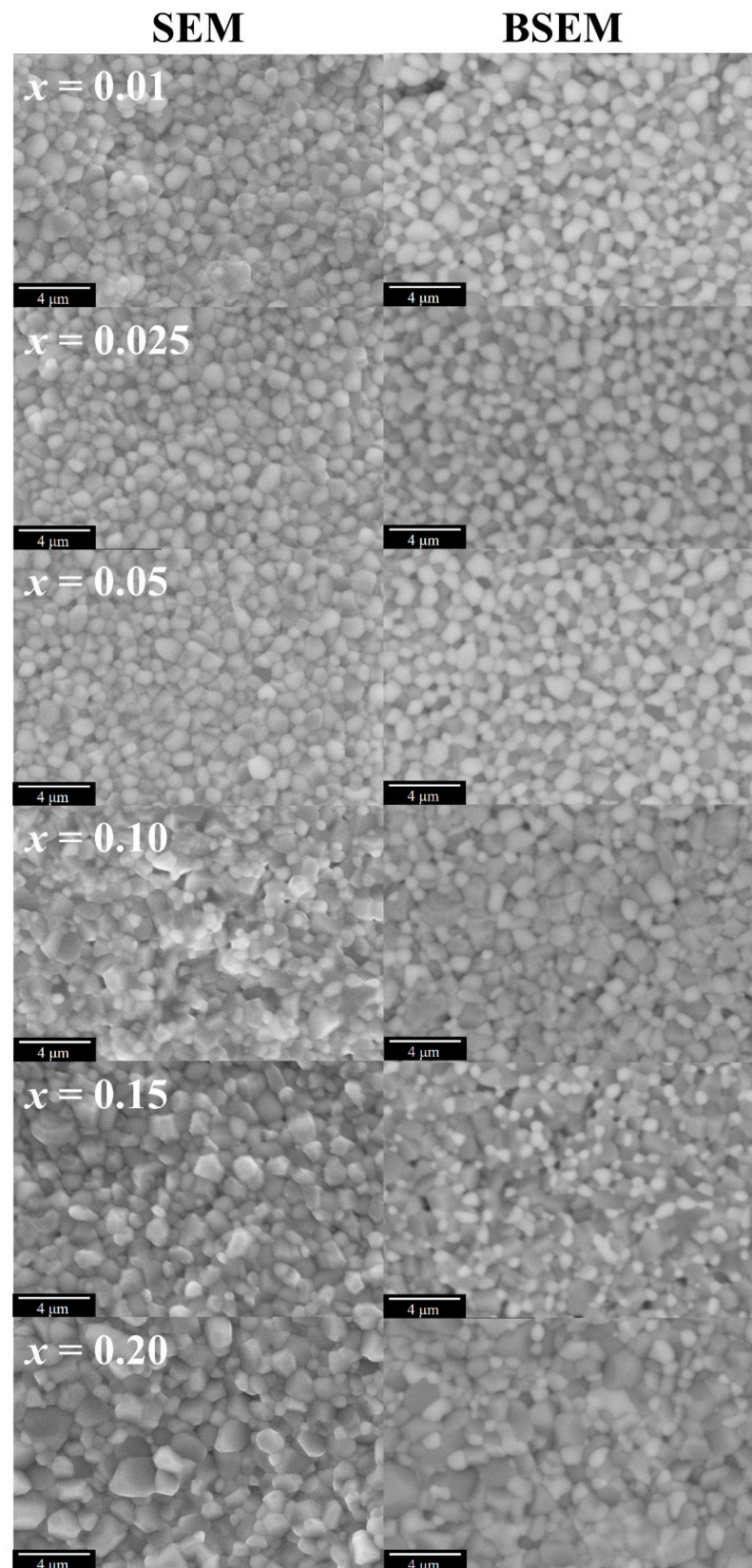


Figure 3. Surface topographies of 60CPO-40PSF_{1-x}B_xO membranes observed by SEM (left) and BSEM (right) after sintered (at 1400 °C for $x = 0.01, 0.025,$ and $0.05,$ 1350 °C for $x = 0.10$ and $0.15,$ 1300 °C for $x = 0.20$) for 5 h.

However, it is difficult to describe the effect of grain size and grain boundary structure on oxygen flux, and it is affected by different oxygen diffusion control steps and conductivity. Generally, larger grains are more favorable for oxygen-permeable membranes controlled by bulk diffusion, while smaller grains produce more grain boundaries, which is beneficial to surface diffusion. However, for the perovskite phase, the grain boundary with higher energy often leads to phase transition and weakens the stability. Zhang group [42] and Yang group [43] added nanoparticles to the grain boundary to restrain the phase transition and prepared stable dual-phase $\text{Ce}_{0.8}\text{Sm}_{0.2}\text{O}_{2-\delta}$ - $\text{SrCo}_{0.9}\text{Nb}_{0.1}\text{O}_{3-\delta}$ and $\text{Ba}_{0.5}\text{Sr}_{0.5}\text{Co}_{0.8}\text{Fe}_{0.2}\text{O}_{3-\delta}$ OTM, respectively. For our OTMs, there are no similar structures in the grain boundary.

Figure 4 shows the EDXS images of the Bi-doped OTMs, which visualize the elemental distribution. All images exhibit a clear complementary elemental distribution in two phases, indicating the well formation of dual-phase OTMs [17,18,21,38]. Ce is mainly distributed in the fluorite phase, while Sr, Fe, and Bi are mainly distributed in the perovskite phase. Pr is distributed in both two phases, but Pr is more abundant in the perovskite phase, so the purple dots in the perovskite region are also significant and right. The homogeneous growth of the dual-phase grains and the highly complementary elemental distribution are evidence that dense dual-phase $60\text{CPO-}40\text{PSF}_{1-x}\text{B}_x\text{O}$ OTMs have been successfully prepared.

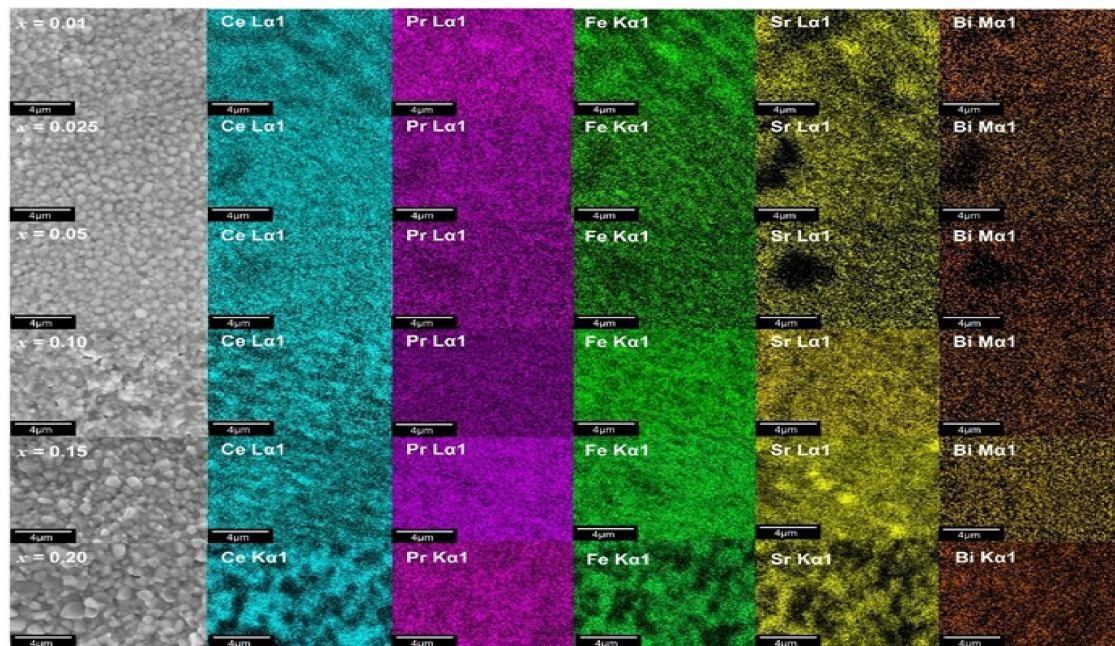


Figure 4. EDXS images of the elemental distribution of $60\text{CPO-}40\text{PSF}_{1-x}\text{B}_x\text{O}$ membranes after sintered for 5 h.

For the dual-phase mixed conductor OTM materials, the relative density and phase distribution have a greater influence on the oxygen flux. A dense lattice structure and smaller porosity can improve the selectivity of oxygen permeability and the structural strength of OTMs. The uniform distribution of the two phases means that there is no enrichment of a single phase [44], which is beneficial to form a continuous conductive network. With the one-pot sol-gel method and multiple grinding processes, we maximize the uniformity of the phase distribution and the relative density of OTMs. Based on the SEM images, we chose the optimal sintering temperature in this case. The OTMs obtained from the optimal temperature all show a suitable density (>90%) and a uniform dual-phase distribution. Compared with the OTMs obtained by the high-temperature solid-state method, there could be more continuous conductive networks and active sites in the interface for the oxygen exchange reaction, which might improve the oxygen permeability [45,46].

3.3. Oxygen Permeation Performance

To investigate the effects of bismuth substitution on the oxygen permeability of 60CPO-40PSF_{1-x}B_xO OTMs, we tested the oxygen permeability for all the OTMs. We plotted J_{O_2} -T curves (Figure 5) in the temperature range of 800–1000 °C. From Figure 5, we can see that all the oxygen permeability through 60CPO-40PSF_{1-x}B_xO dual-phase OTMs increase with increasing temperature and reach a maximum at 1000 °C under either He or CO₂ atmosphere because there are two main steps of oxygen transport in OTMs, bulk diffusion and surface exchange [40], which are influenced by the oxygen partial pressure difference between the feed side and the sweep side of OTMs, the thickness of OTMs, and the temperature. According to the equations of bulk diffusion and surface exchange [47,48], the number of oxygen vacancies increases with increasing temperature, and thereby, the oxygen diffusion can be enhanced in both ways. As shown in Figure 5, the oxygen permeation flux of 60CPO-40PSF_{0.99}B_{0.01}O OTM reaches 0.71 and 0.62 mL·min⁻¹·cm⁻² at 1000 °C under He or CO₂ atmospheres, respectively.

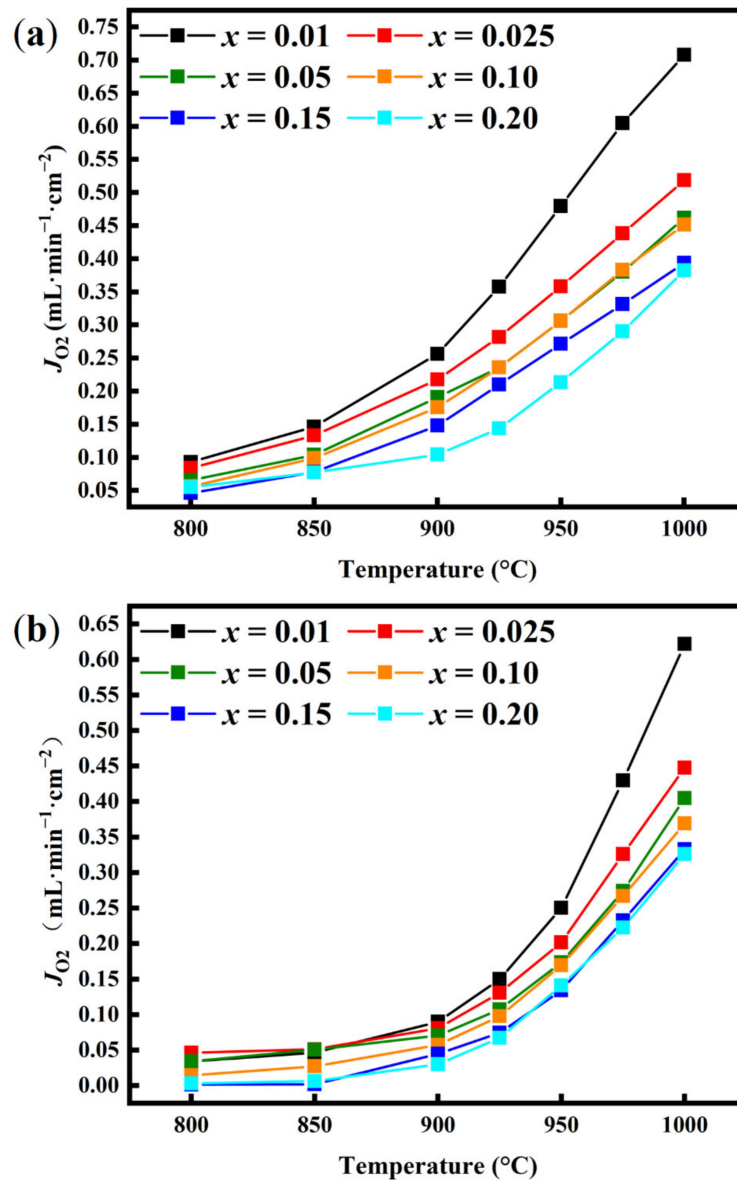


Figure 5. Relationship between oxygen permeation fluxes (J_{O_2}) of 60CPO-40PSF_{1-x}B_xO OTMs and temperature with different sweep gases. Sweep gas: (a) 49 mL·min⁻¹ He. (b) 49 mL·min⁻¹ CO₂. Feed gas: 150 mL·min⁻¹ air. Calibration gas: 1 mL·min⁻¹ Ne. Thickness of OTMs: 0.6 mm.

Figure 6 shows the J_{O_2} - x curves at 1000 °C under He and CO₂ atmospheres. From Figure 6, we can see that the J_{O_2} is much higher than that of the Bi-free 60CPO-40PSFO OTM when $x = 0.01$. However, when $x > 0.01$, as the content of Bi (x) further increases, the J_{O_2} of the Bi-doped OTMs decreases. Overall, the J_{O_2} under the air/He atmosphere is higher than that under the air/CO₂ atmosphere because of the stronger adsorption of CO₂ than that of He. There are several reasons that may explain the enhancement of oxygen permeability of 60CPO-40PSF_{0.99}B_{0.01}O. On the one hand, due to the larger radius of Bi ion and the lower valence state of trivalent, the doped OTM has a smaller tolerance factor and larger lattice parameters, creating more oxygen vacancies and enhancing the oxygen permeability. On the other hand, the larger the Bi dopant content is, the smaller the absolute value of the ABE ($|ABE|$) of B-site (E_{B-O}) in this system (see Figure 6), making the oxygen ion transport easier and thus partially enhancing the oxygen permeability [47,49–52]. E_{B-O} could be calculated by Equation (2) [50]:

$$E_{B-O} = \frac{x}{12} \times \left(\Delta H_{Bi_2O_3} - 2 \times \Delta H_{Bi} - \frac{3}{2} \times D_{O_2} \right) + (1-x) \times E_{Fe-O} \quad (2)$$

where $\Delta H_{Bi_2O_3}$ and ΔH_{Bi} are the enthalpy of formation of one mole of Bi₂O₃ (−573.88 kJ mol^{−1}) and the sublimation energy of Bi metal (207.108 kJ mol^{−1}) at 25 °C [52], respectively. D_{O_2} represents the dissociation energy of O₂ (500.2 kJ mol^{−1}) and E_{Fe-O} is the ABE of the bond Fe-O (−200.6 kJ mol^{−1}) [50].

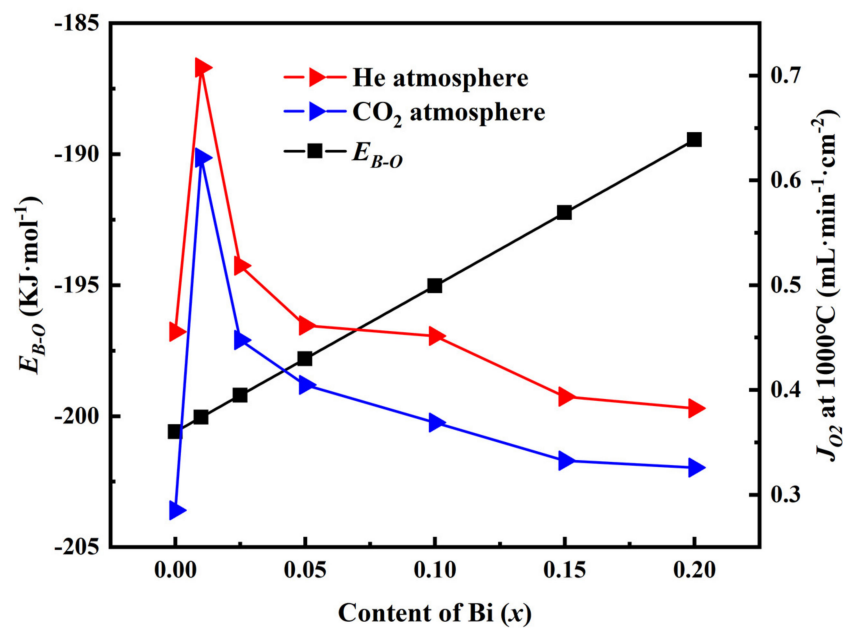


Figure 6. Relationship between oxygen permeation fluxes (J_{O_2}) through 60CPO-40PSF_{1-x}B_xO OTMs under He or CO₂ atmosphere, ABE of B-O bonds, and contents of Bi (x). J_{O_2} for $x = 0$ is from reference [17].

The lower absolute value of the E_{B-O} and formation enthalpies may also explain the decrease in best sintering temperature in Section 3.2 from another perspective. In addition, Bi ion tends to exist as stable Bi³⁺, enhancing the stability of the system. Unlike iron ions with both bivalent and trivalent, where electrons can be rapidly conducted through the change in valence, the doping of Bi weakens the electronic conductivity, such as the results of doping with fixed valence elements such as Al [18,53]. Under He atmosphere, when $x < 0.10$, the enhancement of doping for oxygen permeability is stronger than the reduction brought by the weakening of electronic conductivity. When $x \geq 0.10$, the reduction in electronic conductivity makes the oxygen permeability of the system lower than that of the Bi-free

parent material. However, all Bi-doped OTMs in this system show higher J_{O_2} than that of the parent 60CPO-40PSFO under CO_2 atmosphere. Thus, our findings indicate that a small amount of Bi doping could effectively improve the oxygen permeability of dual-phase OTMs because of the increase in oxygen vacancies and reduction in the $|ABE|$, but over-doped Bi may remarkably reduce the electronic conductivity and consequently abates the oxygen permeability.

3.4. Stabilization

To investigate the stability of 60CPO-40PSF $_{1-x}$ B $_x$ O OTMs under a low oxygen atmosphere or CO_2 atmosphere, the prepared composite powders were calcined at 800, 900, and 1000 °C under pure Ar or CO_2 gas for 24 h. The phase structure of the powders after 24 h calcination under Ar and CO_2 was characterized by XRD after grinding, and the patterns are shown in Figures 7 and 8, respectively. From Figure 7, it can be found that the XRD patterns for the calcination samples are nearly the same as those of the fresh precursor powders. There are no new components or other impurities observed, indicating 60CPO-40PSF $_{1-x}$ B $_x$ O OTMs have suitable structural stability under a low oxygen atmosphere. Moreover, from Figure 8, there are also neither carbonates nor other impurities in the treated 60CPO-40PSF $_{1-x}$ B $_x$ O powders. All the treated powders under pure CO_2 gas are still composed of the CPO phase and PSFBO phase, implying suitable structural stability under the CO_2 atmosphere. Our results are different from the observations in some previous reports [19]. For example, Wang et al. [19] observed the formation of $SrCO_3$ in the Cu-containing $Ce_{0.85}Pr_{0.1}Cu_{0.05}O_{2-\delta}-Pr_xSr_{1-x}Fe_{1-y}Cu_yO_{3-\delta}$ OTMs at 800 °C under pure CO_2 gas due to chemical reactions. Jian Song et al. [26] also reported that the carbonate was generated and adsorbed on the surface of the $BaCo_{0.85}Bi_{0.05}Zr_{0.1}O_{3-\delta}$ OTM, which greatly attenuated the oxygen permeability properties. Since all the 60CPO-40PSF $_{1-x}$ B $_x$ O OTMs do not contain carbonates, their stability can be ensured under the CO_2 atmosphere.

Figure 9 shows the J_{O_2} -t curves of 60CPO-40PSF $_{1-x}$ B $_x$ O OTMs at 1000 °C. All prepared Bi-containing dual-phase OTMs can maintain the J_{O_2} under both He and CO_2 atmospheres over 50 h, indicating excellent stability. However, when the sweep gas was changed to CO_2 , the J_{O_2} of all OTMs declined slightly due to the adsorption of CO_2 on the surfaces of OTMs and affecting the surface exchange of O_2 [17,18,37,54,55]. It is worth mentioning that all these Bi-containing OTMs lost very little oxygen permeation flux in this switching. For example, the J_{O_2} of the champion CPO-PSF $_{0.99}B_{0.01}O$ OTM reached 0.71 and 0.62 mL·min $^{-1}$ ·cm $^{-2}$ under He and CO_2 atmospheres at 1000 °C, respectively. The percentage of loss is only 12.7%, which is more favorable for practical applications compared to other OTMs materials [21,37,38].

To determine the stability, the CPO-PSF $_{0.99}B_{0.01}O$ OTM after the stability test is characterized by SEM and XRD. From Supplementary Figure S2, we can see that two phases are evenly distributed in two sides of the spent 60CPO-40PSFB $_{0.01}O$ membrane. Meanwhile, the element distribution for the feed side and the sweep side of the spent membrane are similar, indicating that there is no element transfer phenomenon in this case. It is different from the previous reports in references [19,40]. On the other hand, we use XRD to further check two sides of the spent membrane. From Supplementary Figure S3, we can see that CPO and PSFBO are two phases as well as glue are the main phases in the spent membranes. No other impurities are observed in the spent membranes, which indicates the spent membranes keep the same crystal structure as the fresh membranes.

In addition, to study the carbon dioxide adsorption behavior of the impurity of different phases, we have performed the TGA experiments for $Ce_{0.9}Pr_{0.1}O_{2-\delta}$, $Pr_{0.6}Sr_{0.4}Fe_{0.99}Bi_{0.01}O_{3-\delta}$ and 60wt.% $Ce_{0.9}Pr_{0.1}O_{2-\delta}$ -40wt.% $Pr_{0.6}Sr_{0.4}Fe_{0.99}Bi_{0.01}O_{3-\delta}$ powders under pure CO_2 atmosphere. From Figure S4, we can see that the mass change of the three kinds of powders was less than 1% when the powders were heated from 300 to 1073 K. Thus, we propose that there is no obvious CO_2 adsorption phenomenon in the three kinds of powders based on the previous finding [56].

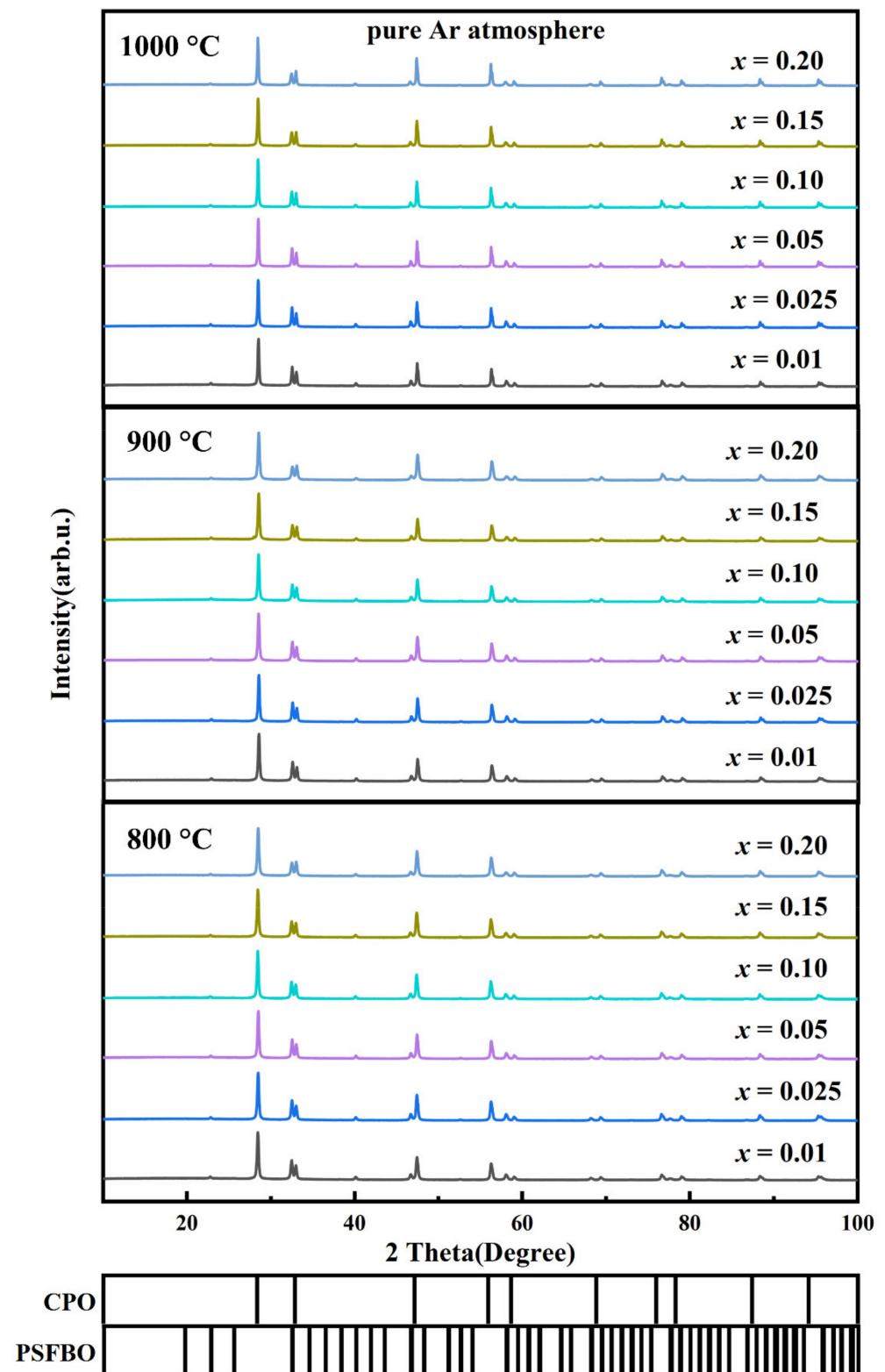


Figure 7. XRD patterns of the obtained 60CPO-40PSF_{1-x}B_xO powders after being calcined under pure Ar gas at 800, 900, and 1000 °C for 24 h.

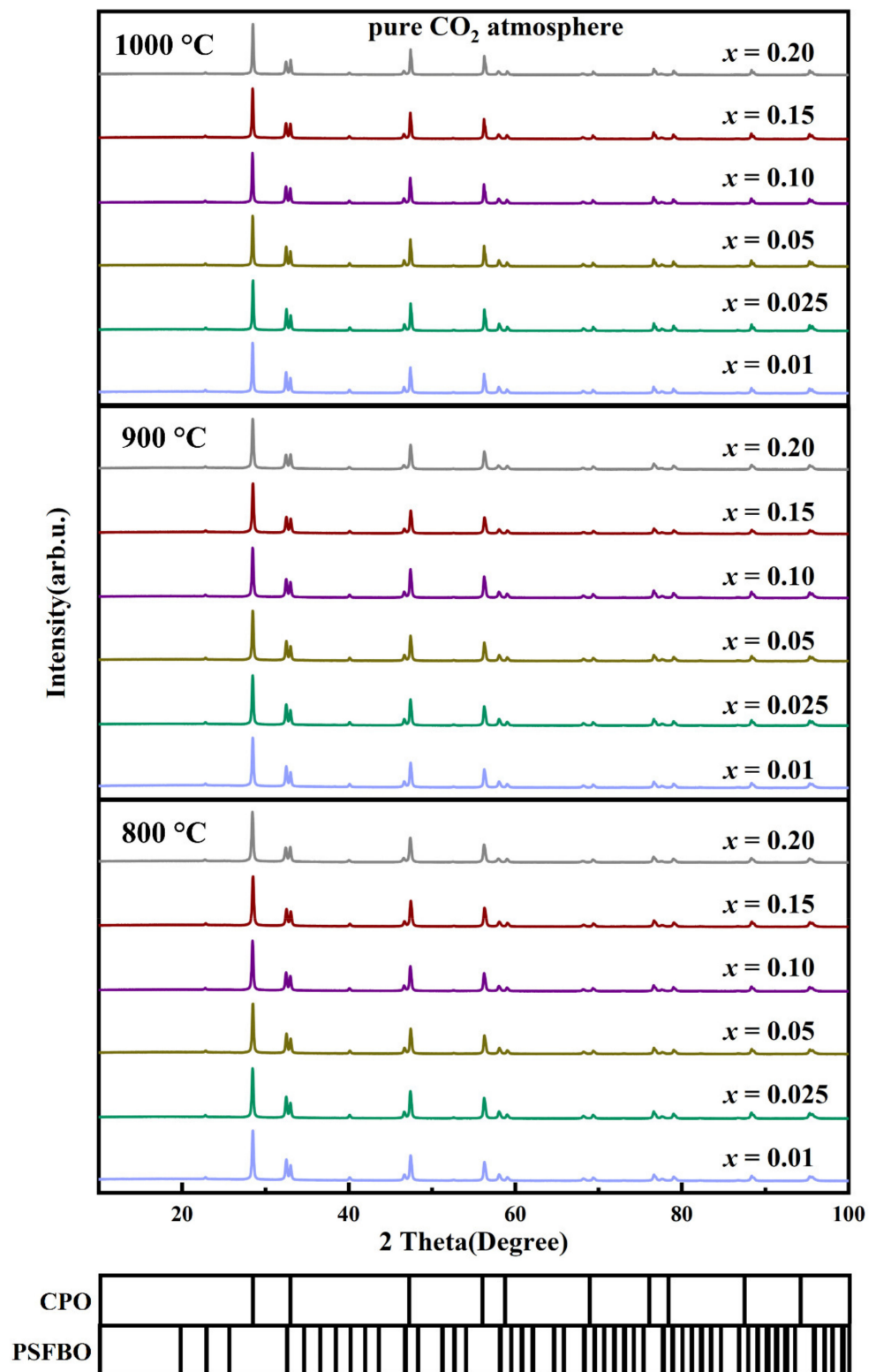


Figure 8. XRD patterns of the obtained 60CPO-40PSF_{1-x}B_xO powders after being calcined under pure CO₂ gas at 800, 900, and 1000 °C for 24 h.

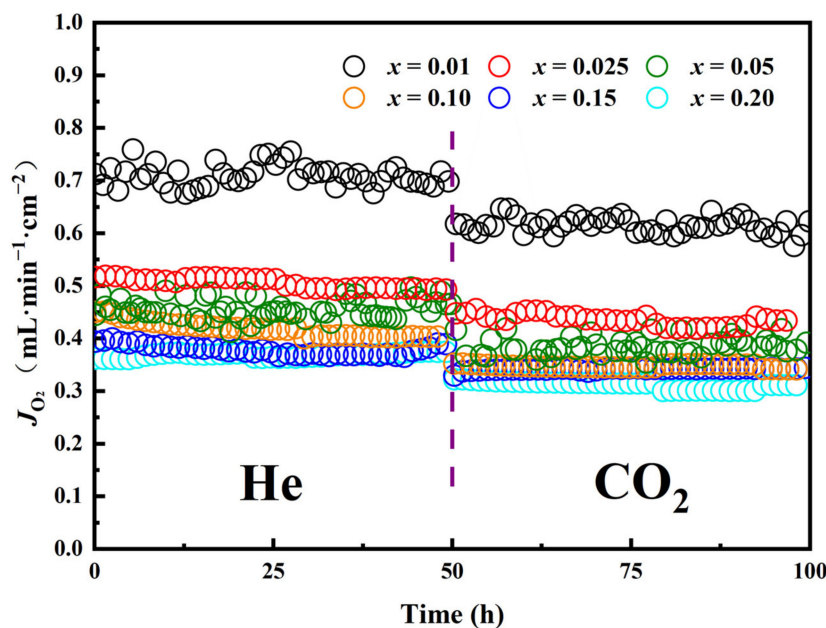


Figure 9. Stability test of 60CPO-40PSF_{1-x}B_xO OTMs at 1000 °C for 50 h: oxygen permeation fluxes (J_{O_2}) as a function of time under He or CO₂ atmosphere.

This CO₂ tolerance is consistent with the absence of carbonate impurities when they are exposed to pure CO₂ gas at high temperatures. This indicates that the dual-phase MIEC OTMs with Bi in the B-site of the perovskite phase (PSFBO) have excellent stability, which is promising for employing in the oxy-fuel process or other CO₂-containing reactions.

4. Conclusions

In this paper, we have successfully synthesized and investigated a series of Bi-doped cobalt-free dual-phase 60CPO-40PSF_{1-x}B_xO ($x = 0.01, 0.025, 0.05, 0.10, 0.15, 0.20$) OTMs. The appropriate content of Bi doping can improve the oxygen permeability of the system, in which the J_{O_2} through the optimal doping composition of CPO-PSF_{0.99}B_{0.01}O OTM reaches 0.71 and 0.62 mL·min⁻¹·cm⁻² under He and CO₂ atmosphere at 1000 °C, respectively. All the 60CPO-40PSF_{1-x}B_xO OTMs can keep stably working in a pure CO₂ atmosphere for more than 50 h without the formation of any carbonate impurities. Our findings provide a suitable prospect in practical usage in industries such as oxygen-enriched combustion and carbon capture.

Supplementary Materials: The following are available online at <https://www.mdpi.com/article/10.3390/pr9101767/s1>, Figure S1: The tolerance factors and sintering temperatures of 60CPO-40PSF_{1-x}B_xO as a function of contents of Bi (x). Figure S2: SEM images and EDXS mappings of two sides of the spent 60CPO-40PSFB0.01O membrane. Figure S3: XRD patterns of two sides of the spent 60CPO-40PSFB0.01O membrane and glue for sealing. Figure S4: TGA results of 60CPO-40PSFB0.01O, CPO and PSFB0.01O powders. Table S1: Density of fresh dual-phase 60CPO-40PSF_{1-x}B_xO membranes.

Author Contributions: H.L., C.Z., and Y.H. (Yanhao Huang) conceived and designed the experiments; C.Z. prepared the samples and the oxygen permeation test; Y.H. (Yiyi He) did the phase stability test under Ar atmosphere; L.Z. and Y.H. (Yiyi He) did the XRD, SEM, and BSEM analysis; P.Y. assisted in preparing the samples; C.Z., Y.H. (Yanhao Huang) and H.L. analyzed all the data and wrote the paper. All authors have read and agreed to the published version of the manuscript.

Funding: This work is supported by the National Natural Science Foundation of China (Grants No. 11922415), Guangdong Basic and Applied Basic Research Foundation (2019A1515011718), the Fundamental Research Funds for the Central Universities (19lgzd03), Key Research & Development Program of Guangdong Province, China (2019B110209003), and the Pearl River Scholarship Program of Guangdong Province Universities and Colleges (20191001).

Acknowledgments: We acknowledge X.P.W. for useful discussions.

Conflicts of Interest: The authors declare no conflict of interest.

References

1. Smart, S.; Lin, C.X.C.; Ding, L.; Thambimuthu, K.; Diniz Da Costa, J.C. Ceramic membranes for gas processing in coal gasification. *Energy Environ. Sci.* **2010**, *3*, 268–278. [[CrossRef](#)]
2. Eichhorn Colombo, K.; Kharton, V.V.; Bolland, O. Simulation of an Oxygen Membrane-Based Gas Turbine Power Plant: Dynamic Regimes with Operational and Material Constraints. *Energy Fuels* **2010**, *24*, 590–608. [[CrossRef](#)]
3. Leo, A.; Liu, S.; Costa, J.C.D.D. Development of mixed conducting membranes for clean coal energy delivery. *Int. J. Greenh. Gas Control* **2009**, *3*, 357–367. [[CrossRef](#)]
4. Zhang, G.; Jin, W.; Xu, N. Design and Fabrication of Ceramic Catalytic Membrane Reactors for Green Chemical Engineering Applications. *Engineering* **2018**, *4*, 848–860. [[CrossRef](#)]
5. Jiang, H.; Wang, H.; Werth, S.; Schiestel, T.; Caro, J. Simultaneous Production of Hydrogen and Synthesis Gas by Combining Water Splitting with Partial Oxidation of Methane in a Hollow-Fiber Membrane Reactor. *Angew. Chem. Int. Ed.* **2008**, *47*, 9341–9344. [[CrossRef](#)]
6. Luo, H.; Wei, Y.; Jiang, H.; Yuan, W.; Lv, Y.; Caro, J.; Wang, H. Performance of a ceramic membrane reactor with high oxygen flux Ta-containing perovskite for the partial oxidation of methane to syngas. *J. Membr. Sci.* **2010**, *350*, 154–160. [[CrossRef](#)]
7. Cao, Z.; Jiang, H.; Luo, H.; Baumann, S.; Meulenberg, W.A.; Assmann, J.; Mleczko, L.; Liu, Y.; Caro, J. Natural Gas to Fuels and Chemicals: Improved Methane Aromatization in an Oxygen-Permeable Membrane Reactor. *Angew. Chem. Int. Ed.* **2013**, *52*, 13794–13797. [[CrossRef](#)]
8. Alqaheem, Y.; Thursfield, A.; Zhang, G.; Metcalfe, I.S. The impact of sulfur contamination on the performance of $\text{La}_{0.6}\text{Sr}_{0.4}\text{Co}_{0.2}\text{Fe}_{0.8}\text{O}_{3-\delta}$ oxygen transport membranes. *Solid State Ion.* **2014**, *262*, 262–265. [[CrossRef](#)]
9. Liu, S.; Lu, X.F.; Xiao, J.; Wang, X.; Lou, X.W. Bi_2O_3 Nanosheets Grown on Multi-Channel Carbon Matrix to Catalyze Efficient CO_2 Electroreduction to HCOOH . *Angew. Chem. Int. Ed.* **2019**, *58*, 13828–13833. [[CrossRef](#)]
10. Waindich, A.; Möbius, A.; Müller, M. Corrosion of $\text{Ba}_{1-x}\text{Sr}_x\text{Co}_{1-y}\text{Fe}_y\text{O}_{3-\delta}$ and $\text{La}_{0.3}\text{Ba}_{0.7}\text{Co}_{0.2}\text{Fe}_{0.8}\text{O}_{3-\delta}$ materials for oxygen separating membranes under Oxycoal conditions. *J. Membr. Sci.* **2009**, *337*, 182–187. [[CrossRef](#)]
11. Xie, J.; Ju, Y.-W.; Ishihara, T. Influence of sulfur impurities on the stability of $\text{La}_{0.6}\text{Sr}_{0.4}\text{Co}_{0.2}\text{Fe}_{0.8}\text{O}_3$ cathode for solid oxide fuel cells. *Solid State Ion.* **2013**, *249–250*, 177–183. [[CrossRef](#)]
12. Venkatalaxmi, A.; Padmavathi, B.S.; Amaranath, T. A general solution of unsteady Stokes equations. *Fluid Dyn. Res.* **2004**, *35*, 229–236. [[CrossRef](#)]
13. Zhang, C.; Sunarso, J.; Liu, S. Designing CO_2 -resistant oxygen-selective mixed ionic–electronic conducting membranes: Guidelines, recent advances, and forward directions. *Chem. Soc. Rev.* **2017**, *46*, 2941–3005. [[CrossRef](#)] [[PubMed](#)]
14. Schlehner, D.; Wessel, E.; Singheiser, L.; Markus, T. Long-term operation of a $\text{La}_{0.58}\text{Sr}_{0.4}\text{Co}_{0.2}\text{Fe}_{0.8}\text{O}_{3-\delta}$ -membrane for oxygen separation. *J. Membr. Sci.* **2010**, *351*, 16–20. [[CrossRef](#)]
15. Shao, Z.; Dong, H.; Xiong, G.; Cong, Y.; Yang, W. Performance of a mixed-conducting ceramic membrane reactor with high oxygen permeability for methane conversion. *J. Membr. Sci.* **2001**, *183*, 181–192. [[CrossRef](#)]
16. Partovi, K.; Geppert, B.; Liang, F.; Rüscher, C.H.; Caro, J. Effect of the B-Site Composition on the Oxygen Permeability and the CO_2 Stability of $\text{Pr}_{0.6}\text{Sr}_{0.4}\text{Co}_x\text{Fe}_{1-x}\text{O}_{3-\delta}$ ($0.0 \leq x \leq 1.0$) Membranes. *Chem. Mater.* **2015**, *27*, 2911–2919. [[CrossRef](#)]
17. Luo, H.; Jiang, H.; Klande, T.; Cao, Z.; Liang, F.; Wang, H.; Caro, J. Novel Cobalt-Free, Noble Metal-Free Oxygen-Permeable $40\text{Pr}_{0.6}\text{Sr}_{0.4}\text{FeO}_{3-\delta}-60\text{Ce}_{0.9}\text{Pr}_{0.1}\text{O}_{2-\delta}$ Dual-Phase Membrane. *Chem. Mater.* **2012**, *24*, 2148–2154. [[CrossRef](#)]
18. Shi, L.; Wang, S.; Lu, T.; He, Y.; Yan, D.; Lan, Q.; Xie, Z.; Wang, H.; Boubeche, M.; Luo, H. Effects of Al content on the oxygen permeability through dual-phase membrane $60\text{Ce}_{0.9}\text{Pr}_{0.1}\text{O}_{2-\delta}-40\text{Pr}_{0.6}\text{Sr}_{0.4}\text{Fe}_{1-x}\text{Al}_x\text{O}_3$. *Ceram. Int.* **2019**, *45*, 20033–20039. [[CrossRef](#)]
19. Wang, X.; Huang, Y.; Li, D.; Zeng, L.; He, Y.; Boubeche, M.; Luo, H. High oxygen permeation flux of cobalt-free Cu-based ceramic dual-phase membranes. *J. Membr. Sci.* **2021**, *633*, 119403. [[CrossRef](#)]
20. Jeong, N.C.; Lee, J.S.; Tae, E.L.; Lee, Y.J.; Yoon, K.B. Acidity Scale for Metal Oxides and Sanderson’s Electronegativities of Lanthanide Elements. *Angew. Chem. Int. Ed.* **2008**, *47*, 10128–10132. [[CrossRef](#)]
21. Liang, F.; Luo, H.; Partovi, K.; Ravkina, O.; Cao, Z.; Liu, Y.; Caro, J. A novel CO_2 -stable dual phase membrane with high oxygen permeability. *Chem. Commun.* **2014**, *50*, 2451–2454. [[CrossRef](#)] [[PubMed](#)]
22. Huang, Y.; Zhang, C.; Wang, X.; Li, D.; Zeng, L.; He, Y.; Yu, P.; Luo, H. High CO_2 resistance of indium-doped cobalt-free 60 wt.% $\text{Ce}_{0.9}\text{Pr}_{0.1}\text{O}_{2-\delta}$ -40 wt.% $\text{Pr}_{0.6}\text{Sr}_{0.4}\text{Fe}_{1-x}\text{In}_x\text{O}_{3-\delta}$ oxygen transport membranes. *Ceram. Int.* **2021**. [[CrossRef](#)]
23. Luo, H.; Klande, T.; Cao, Z.; Liang, F.; Wang, H.; Caro, J. A CO_2 -stable reduction-tolerant Nd-containing dual phase membrane for oxyfuel CO_2 capture. *J. Mater. Chem. A* **2014**, *2*, 7780–7787. [[CrossRef](#)]
24. Partovi, K.; Bittner, M.; Caro, J. Novel CO_2 -tolerant Al-containing membranes for high-temperature oxygen separation. *J. Mater. Chem. A* **2015**, *3*, 24008–24015. [[CrossRef](#)]
25. Wang, Z.; Kathiraser, Y.; Kawi, S. High performance oxygen permeable membranes with Nb-doped $\text{BaBi}_{0.05}\text{Co}_{0.95}\text{O}_{3-\delta}$ perovskite oxides. *J. Membr. Sci.* **2013**, *431*, 180–186. [[CrossRef](#)]
26. Song, J.; Qiu, Z.; Gao, J.; Tan, X.; Sunarso, J.; Wang, S.; Liu, S. CO_2 erosion of $\text{BaCo}_{0.85}\text{Bi}_{0.05}\text{Zr}_{0.1}\text{O}_{3-\delta}$ perovskite membranes under oxygen permeating conditions. *Sep. Purif. Technol.* **2018**, *207*, 133–141. [[CrossRef](#)]
27. Pyykko, P. Relativistic effects in structural chemistry. *Chem. Rev.* **1988**, *88*, 563–594. [[CrossRef](#)]

28. Yan, T.; Li, N.; Wang, L.; Ran, W.; Duchesne, P.N.; Wan, L.; Nguyen, N.T.; Wang, L.; Xia, M.; Ozin, G.A. Bismuth atom tailoring of indium oxide surface frustrated Lewis pairs boosts heterogeneous CO₂ photocatalytic hydrogenation. *Nat. Commun.* **2020**, *11*, 6095. [[CrossRef](#)]
29. Yashima, M.; Ishimura, D. Crystal structure and disorder of the fast oxide-ion conductor cubic Bi₂O₃. *Chem. Phys. Lett.* **2003**, *378*, 395–399. [[CrossRef](#)]
30. Wachsman, E.D. Effect of oxygen sublattice order on conductivity in highly defective fluorite oxides. *J. Eur. Ceram. Soc.* **2004**, *24*, 1281–1285. [[CrossRef](#)]
31. Sanna, S.; Esposito, V.; Andreasen, J.W.; Hjelm, J.; Zhang, W.; Kasama, T.; Simonsen, S.B.; Christensen, M.; Linderroth, S.; Pryds, N. Enhancement of the chemical stability in confined δ-Bi₂O₃. *Nat. Mater.* **2015**, *14*, 500–504. [[CrossRef](#)] [[PubMed](#)]
32. Bothwell, J.M.; Krabbe, S.W.; Mohan, R.S. Applications of bismuth(iii) compounds in organic synthesis. *Chem. Soc. Rev.* **2011**, *40*, 4649–4707. [[CrossRef](#)]
33. Deng, P.; Wang, H.; Qi, R.; Zhu, J.; Chen, S.; Yang, F.; Zhou, L.; Qi, K.; Liu, H.; Xia, B.Y. Bismuth Oxides with Enhanced Bismuth–Oxygen Structure for Efficient Electrochemical Reduction of Carbon Dioxide to Formate. *ACS Catal.* **2020**, *10*, 743–750. [[CrossRef](#)]
34. Momma, K.; Izumi, F. VESTA: A three-dimensional visualization system for electronic and structural analysis. *J. Appl. Crystallogr.* **2008**, *41*, 653–658. [[CrossRef](#)]
35. Luo, H.; Jiang, H.; Efimov, K.; Caro, J.; Wang, H. Influence of the preparation methods on the microstructure and oxygen permeability of a CO₂-stable dual phase membrane. *AIChE J.* **2011**, *57*, 2738–2745. [[CrossRef](#)]
36. Kharton, V.V.; Kovalevsky, A.V.; Viskup, A.P.; Figueiredo, F.M.; Yaremchenko, A.A.; Naumovich, E.N.; Marques, F.M.B. Oxygen Permeability of Ce_{0.8}Gd_{0.2}O_{2-δ}-La_{0.7}Sr_{0.3}MnO_{3-δ} Composite Membranes. *J. Electrochem. Soc.* **2000**, *147*, 2814. [[CrossRef](#)]
37. Wang, X.; Shi, L.; Huang, Y.; Zeng, L.; Boubeche, M.; Li, D.; Luo, H. CO₂-Tolerant Oxygen Permeation Membranes Containing Transition Metals as Sintering Aids with High Oxygen Permeability. *Processes* **2021**, *9*, 528. [[CrossRef](#)]
38. Shi, L.; Wang, S.; Lu, T.; He, Y.; Yan, D.; Lan, Q.; Xie, Z.; Wang, H.; Li, M.-R.; Caro, J.; et al. High CO₂-tolerance oxygen permeation dual-phase membranes Ce_{0.9}Pr_{0.1}O₂-Pr_{0.6}Sr_{0.4}Fe_{0.8}Al_{0.2}O₃. *J. Alloy. Compd.* **2019**, *806*, 500–509. [[CrossRef](#)]
39. Goldschmidt, V.M. Die Gesetze der Krystallochemie. *Die Nat.* **1926**, *14*, 477–485. [[CrossRef](#)]
40. Geffroy, P.M.; Reichmann, M.; Kilmann, L.; Jouin, J.; Richet, N.; Chartier, T. Identification of the rate-determining step in oxygen transport through La_{1-x}Sr_xFe_{1-y}Ga_yO_{3-δ} perovskite membranes. *J. Membr. Sci.* **2015**, *476*, 340–347. [[CrossRef](#)]
41. Luo, H.; Jiang, H.; Efimov, K.; Liang, F.; Wang, H.; Caro, J. CO₂-Tolerant Oxygen-Permeable Fe₂O₃-Ce_{0.9}Gd_{0.1}O_{2-δ} Dual Phase Membranes. *Ind. Eng. Chem. Res.* **2011**, *50*, 13508–13517. [[CrossRef](#)]
42. Zhang, Z.; Ning, K.; Xu, Z.; Zheng, Q.; Tan, J.; Liu, Z.; Wu, Z.; Zhang, G.; Jin, W. Highly efficient preparation of Ce_{0.8}Sm_{0.2}O_{2-δ}-SrCo_{0.9}Nb_{0.1}O_{3-δ} dual-phase four-channel hollow fiber membrane via one-step thermal processing approach. *J. Membr. Sci.* **2021**, *620*, 118752. [[CrossRef](#)]
43. Liu, Y.; Zhu, X.; Li, M.; O’Hayre, R.P.; Yang, W. Nanoparticles at Grain Boundaries Inhibit the Phase Transformation of Perovskite Membrane. *Nano Lett.* **2015**, *15*, 7678–7683. [[CrossRef](#)]
44. Li, Q.; Zhu, X.; He, Y.; Cong, Y.; Yang, W. Effects of sintering temperature on properties of dual-phase oxygen permeable membranes. *J. Membr. Sci.* **2011**, *367*, 134–140. [[CrossRef](#)]
45. Zhu, X.; Yang, W. Microstructural and Interfacial Designs of Oxygen-Permeable Membranes for Oxygen Separation and Reaction–Separation Coupling. *Adv. Mater.* **2019**, *31*, 1902547. [[CrossRef](#)]
46. Luo, H.; Efimov, K.; Jiang, H.; Feldhoff, A.; Wang, H.; Caro, J. CO₂-Stable and Cobalt-Free Dual-Phase Membrane for Oxygen Separation. *Angew. Chem. Int. Ed.* **2011**, *50*, 759–763. [[CrossRef](#)] [[PubMed](#)]
47. Shao, Z.; Xiong, G.; Cong, Y.; Yang, W. Synthesis and oxygen permeation study of novel perovskite-type BaBi_xCo_{0.2}Fe_{0.8-x}O_{3-δ} ceramic membranes. *J. Membr. Sci.* **2000**, *164*, 167–176. [[CrossRef](#)]
48. Balaguer, M.; Solís, C.; Serra, J.M. Structural–Transport Properties Relationships on Ce_{1-x}Ln_xO_{2-δ} System (Ln = Gd, La, Tb, Pr, Eu, Er, Yb, Nd) and Effect of Cobalt Addition. *J. Phys. Chem. C* **2012**, *116*, 7975–7982. [[CrossRef](#)]
49. Du, Z.; Ma, Y.; Zhao, H.; Li, K.; Lu, Y. High CO₂-tolerant and Cobalt-free dual-phase membranes for pure oxygen separation. *J. Membr. Sci.* **2019**, *574*, 243–251. [[CrossRef](#)]
50. Konysheva, E.Y.; Xu, X.; Irvine, J.T.S. On the Existence of A-Site Deficiency in Perovskites and Its Relation to the Electrochemical Performance. *Adv. Mater.* **2012**, *24*, 528–532. [[CrossRef](#)]
51. Lide, D.R. *CRC Handbook of Chemistry and Physics*; CRC Press: Boca Raton, FL, USA, 2004; Volume 85.
52. Dean, J.A. *Lange’s Handbook of Chemistry*; McGraw-Hill Education: New York, NY, USA, 1990; Volume 5, pp. 687–688.
53. Liu, X.Q.; Yang, W.Z.; Song, C.L.; Chen, X.M. Dielectric relaxation in LaSrCo_{1-x}Al_xO₄ ceramics. *Appl. Phys. A* **2010**, *100*, 1131–1135. [[CrossRef](#)]
54. Zhu, X.; Liu, H.; Cong, Y.; Yang, W. Novel dual-phase membranes for CO₂ capture via an oxyfuel route. *Chem. Commun.* **2012**, *48*, 251–253. [[CrossRef](#)] [[PubMed](#)]
55. Zhu, J.; Guo, S.; Chu, Z.; Jin, W. CO₂-tolerant oxygen-permeable perovskite-type membranes with high permeability. *J. Mater. Chem. A* **2015**, *3*, 22564–22573. [[CrossRef](#)]
56. Wang, Z.; Liu, W.; Wu, Y.; Sun, W.; Liu, W.; Wang, C. A novel cobalt-free CO₂-stable perovskite-type oxygen permeable membrane. *J. Membr. Sci.* **2019**, *573*, 504–510. [[CrossRef](#)]